

Unraveling the Eclipse Mechanism of a Binary Millisecond Pulsar Using Broadband Radio Spectra

DEVOJYOTI KANSABANIK ¹, BHASWATI BHATTACHARYYA ¹, JAYANTA ROY ¹ AND BENJAMIN STAPPERS ²

¹*National Centre for Radio Astrophysics, Tata Institute of Fundamental Research, Pune University, Pune 411007, India*

²*Jodrell Bank Centre for Astrophysics, Department of Physics and Astronomy, The University of Manchester*

(Received June 12, 2021; Revised July 27, 2021; Accepted July 27, 2021; Published October 13, 2021)

Submitted to ApJ

ABSTRACT

The frequency dependent eclipses of the radio emission from millisecond pulsars (MSPs) in compact binary systems provide an opportunity to understand the eclipse mechanism and to determine the nature of the eclipsing medium. We combine multifrequency observations from the upgraded Giant Metrewave Radio Telescope (uGMRT) and model the broadband radio spectrum in the optically thick to thin transition regime to constrain the eclipse mechanism. The best-fit model to the eclipse phase spectra favors synchrotron absorption by relativistic electrons. We are able to strongly constrain the frequency of onset of the eclipse to 345 ± 5 MHz, which is an order of magnitude more precise than previous estimates. The dependence on the magnetic field strength of synchrotron absorption allowed us to estimate the magnetic field strength of the eclipse medium to be ~ 13 G, which is very similar to the values obtained by considering a pressure balance between the incident pulsar wind and the stellar wind of the companion. Applying this method to other millisecond binary pulsars will enable us to determine if the eclipse mechanisms are all the same and also estimate the wind and magnetic field properties of the companion stars. The method could also be applied to other systems where pulsars interact with companion winds in binary systems and in all cases it will lead to a better understanding of the evolutionary processes.

Keywords: Binary pulsars (153), Interacting binary stars (801), Close binary stars (254), Radio pulsars (1353), Radio spectroscopy (1359), Millisecond pulsars (1062), Eclipses (442), Eclipsing binary stars (444)

1. INTRODUCTION

Millisecond pulsars (MSPs) are rapidly rotating neutron stars that are spun up to spin periods of a few milliseconds via the transfer of angular momentum through accretion of stellar material from the companion star (Bhattacharya 1996). MSPs found in compact binary orbits (orbital period; $P_b \leq 10$ hours) around a low-mass companion ($M_C \leq 0.1 M_\odot$) are important for understanding the formation of MSPs and the links between binary and isolated MSPs (Roberts 2013; Benvenuto et al. 2014). Most of the MSPs in compact orbits show frequency dependent eclipses of the radio emission

from the pulsar when the companion star comes close to the line-of-sight (LOS). It is believed that eclipses are caused by either the material blown from the companion star by the pulsar wind or the material inside the pulsar wind itself. Following the discovery of the first eclipsing MSP B1957+20 (Fruchter et al. 1990), eclipse mechanism studies were performed for a handful of eclipsing binary pulsars (e.g PSR J1227–4853 (Roy et al. 2015; Kudale et al. 2020), PSR J1544+4937 (Bhattacharyya et al. 2013), PSR J1744–24A (Lyne et al. 1990), PSR J1810+1744 (Polzin et al. 2018), PSR B1957+20 (Fruchter et al. 1990; Fruchter et al. 1988; Polzin et al. 2020) and PSR J2051–0827 (Stappers et al. 1998; Polzin et al. 2019)). The majority of the previous studies were limited to narrow bandwidth observations at the frequencies where the eclipse medium is

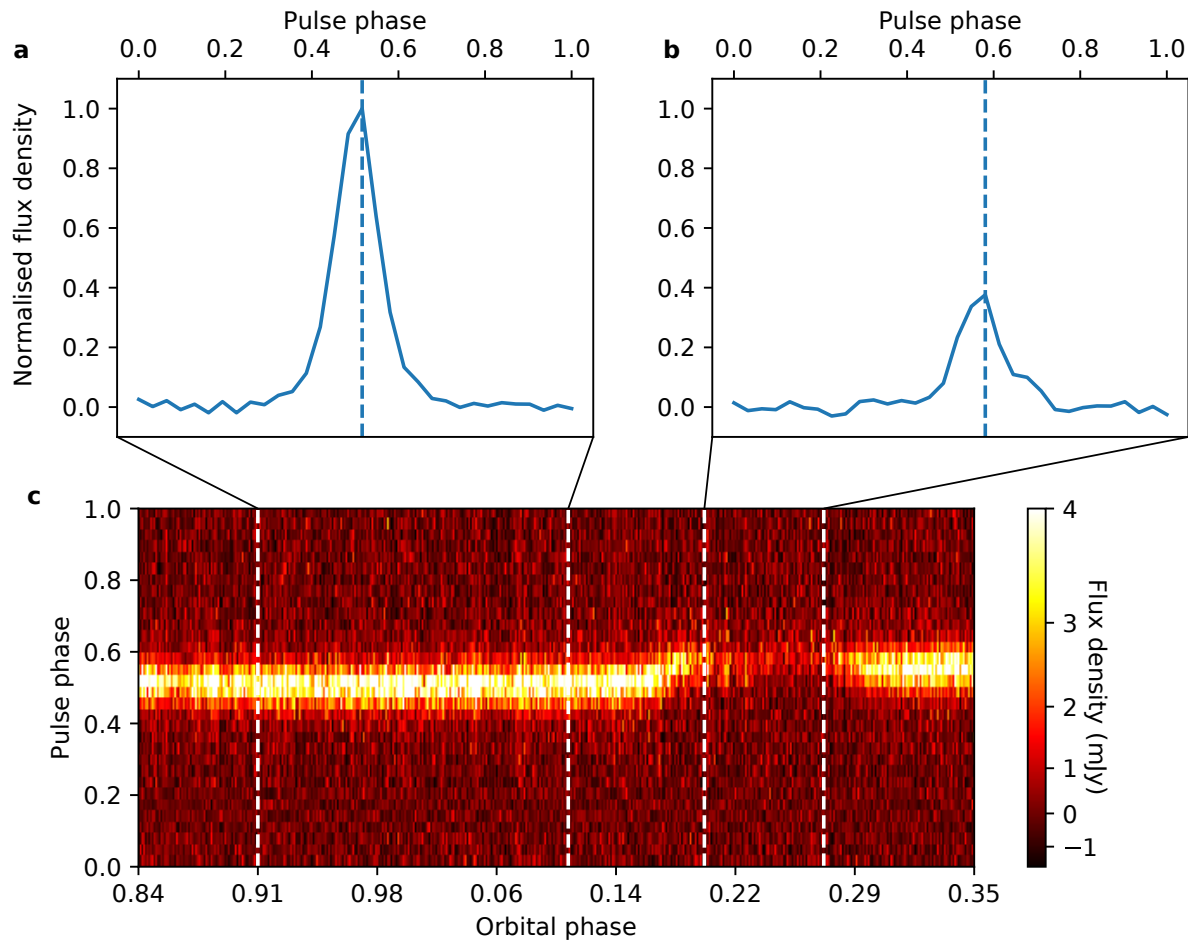


Figure 1. Pulsed flux density variation of PSR J1544+4937 in the FEP and NEP at band 3 on 2018 February 6. (a),(b) Average pulse profile in the NEP (orbital phase 0.91–0.10) and the FEP (orbital phase 0.19–0.27) are shown respectively. Both the pulse profiles in the NEP and FEP are normalized with respect to the NEP peak flux density. The flux density at the FEP is reduced about 60% from the NEP flux density. The peak of the pulse profile is shifted $\sim 100\mu\text{s}$ in the FEP (from pulse phase 0.5 to 0.55) due to the observed excess electron column density in the eclipse phase. (c) Variation of the pulsed flux density with orbital phase is shown. The flux density is shown by the color scale. At the FEP there is a significant reduction in the flux density associated with excess time delay in pulse arrival times.

optically thick and the pulsar radiation is completely eclipsed. Thus, these investigations could only probe the eclipse boundaries implying that the eclipse mechanism and the eclipse medium properties had to be inferred indirectly. Simultaneous multifrequency studies have also been undertaken, but they were typically at widely separated frequencies and the spectral evolution due to the eclipse medium was difficult to constrain. Detailed investigation of the frequency dependent eclipsing with wide bandwidth observations are therefore needed to probe the physical conditions near the superior conjunction (Freire 2005) which could be significantly different than near the eclipse boundaries.

The majority of the previous studies concluded that the eclipse at lower frequencies (≤ 1 GHz) may be caused by cyclotron/synchrotron absorption (Thompson et al. 1994). Thus, the magnetic field is an important physical parameters of the eclipse medium in causing the eclipse by cyclotron/synchrotron absorption. Previous studies (Fruchter et al. 1990; Li et al. 2019; Crowter et al. 2020) estimated the magnetic field strength of the eclipse medium at the eclipse boundaries. The estimated magnetic field strength was a few milligauss and at least two orders of magnitude smaller than the characteristic magnetic field strength (B_E) calculated using the pressure balance between the pulsar wind and the stellar wind of the companion. One possible reason may be the differ-

ent eclipse medium properties at different orbital phases. Electron column density variations with orbital phase in different eclipsing MSPs have been reported by previous studies (Fruchter et al. 1988; Stappers et al. 1998; Bhattacharyya et al. 2013; Polzin et al. 2018). Similarly the magnetic field strength of the eclipse medium may also vary as we move away from the superior conjunction of the companion (Khechinashvili et al. 2000). Since the previous estimations of magnetic field strengths were at the eclipse boundaries, it is necessary to estimate the properties of the eclipse medium directly at the superior conjunction.

The availability of the new wide bandwidth facilities like the Parkes ultra-wideband receiver (Hobbs et al. 2020, UWL) and the upgraded Giant Metrewave Radio Telescope (Gupta et al. 2017, uGMRT) allows one to probe the eclipse medium while transitioning from the optically thick to the optically thin regime. Although some previous studies (Polzin et al. 2019; Polzin et al. 2020) used wide bandwidth observations with the Parkes and uGMRT, they did not use the broadband radio spectrum to probe the eclipse mechanism. Here we demonstrate a new method that utilizes the broadband radio spectrum, a crucial discriminator between different eclipse mechanisms, for probing the eclipse mechanism. We have applied this new method to the eclipsing MSP J1544+4937 (Bhattacharyya et al. 2013) to provide strong constraints on the eclipse mechanism and also to estimate the physical parameters of the eclipse medium at the superior conjunction. The details of the observations and the data analysis are discussed in Section 2. In Section 3, our findings on eclipse mechanisms and eclipse medium properties for PSR J1544+4937 are detailed. Section 4 presents a summary and discussion of the prospects for future implementation of this method to other systems.

2. OBSERVATION AND DATA ANALYSIS

A crucial discriminator between the different eclipse mechanisms is the frequency dependence of the eclipse duration, and it is apparent from the earlier narrow bandwidth observations that wide bandwidth observations are needed to capture any changes in the spectral properties of the received emission due to the eclipse medium. For this study we chose PSR J1544+4937 (Bhattacharyya et al. 2013), an MSP discovered with the GMRT (Swarup 1991), which is in a compact binary orbit ($P_b \approx 2.9$ hours). Previous investigations with the GMRT software backend (Roy et al. 2010) using 32 MHz of bandwidth indicates that PSR J1544+4937 exhibits frequency dependent eclipsing. Although the radio emission of the pulsar is obscured near the companion's su-

perior conjunction at 306–338 MHz, it is detected at 591–623 MHz (Bhattacharyya et al. 2013). This previous study reported an uncertainty of 250 MHz on the frequency where radio emission from the pulsar is no longer detected. To more accurately determine this transition frequency we used the wide bandwidth capabilities of the uGMRT to observe PSR J1544+4937 at 300–500 MHz (band 3) and 650–850 MHz (band 4). We used high time resolution non-imaging data in total intensity for this study.

2.1. Observation

The observations were performed with the uGMRT (Gupta et al. 2017), which is a radio interferometric array consisting of 30 dishes. We performed observation on three different epochs. Observations on 2018 February 6 and 2018 April 17 were performed by splitting the total number of antennas into two sub-arrays at 300–500 MHz and 650–850 MHz, whereas the observations on 2018 May 7 were performed using all antennas at 300–500 MHz. The observations were carried out in phased array mode where the spectral voltage signals from different antennas are coherently added together to form a single dish using the whole array. Coherent beam filterbank data at 48.28 kHz frequency resolution with 4096 frequency channels were recorded at every 81.92 μ s. The observations were scheduled in such a way that the full eclipse phase (FEP) was covered.

2.2. Data processing

We have used the GMRT pulsar tool [GPTOOL (Chowdhury A. et al., in preparation) to perform automated radio frequency interference (RFI) mitigation. The data were then corrected for interstellar dispersion with incoherent dedispersion (Lorimer & Kramer 2004) and then folded with the known ephemeris of the pulsar using DSPSR (van Straten & Bailes 2010). We have used TEMPO2 (Hobbs et al. 2006; Edwards et al. 2006) to calculate the difference between the observed and computed pulse time of arrivals (TOAs) using the known ephemeris of the pulsar derived from non-eclipse phase (NEP) TOAs. Then the excess electron column density in the eclipse medium is measured directly from the observed excess time delay of the pulsed emission (Lorimer & Kramer 2004) as

$$DM_{ex}(\text{pc cm}^{-3}) = 2.4 \times 10^{-10} t_{ex}(\mu\text{s}) f(\text{MHz})^2 \quad (1)$$

where t_{ex} is the excess observed time delay, DM_{ex} is the excess dispersion measure (DM) calculated from the t_{ex} and f is the observing frequency in MHz. The excess DM is then converted to excess electron column density as

$$N_e(\text{cm}^{-2}) = 3 \times 10^{18} \times DM(\text{pc cm}^{-3}) \quad (2)$$

The observed data are flux calibrated using a flux calibrator 3C 286 (Appendix A.1). We used the flux calibrated pulse averaged flux density for the rest of the work (Appendix A.2).

2.3. Variation of flux density and electron column density across the eclipse phase

The flux density reduced during the eclipse phase. In Figure 1c, we show the variation of pulsed flux density in band 3 as a function of orbital phase. We define the orbital phase 0.19–0.27 around superior conjunction ($\phi_b = 0.25$) to be FEP and 0.91–1.0 to be a part of the NEP. There is an approximate 60% reduction in the received pulse flux density in the FEP and a corresponding average delay in the arrival time of the pulses of 100 μ s (Figure 1a,b). In Figure 2a, we show the variation in the delay in the pulse TOA in band 3 and the corresponding excess electron column density throughout the eclipse phase for three different epochs (Section 2). The variation in flux density, normalized with respect to the NEP flux density, is shown in Figure 2b. We have marked three different regions in the eclipse phase; eclipse ingress phase (EIP), FEP and eclipse egress phase (EEP) in Figure 2. In contrast to what was seen in band 3, in band 4, we detect no change in the observed flux density between the FEP and NEP greater than our noise limit of $\sim 100 \mu$ Jy.

2.4. Spectra at different orbital phases

To further study the frequency dependence of the flux density of the pulsar during the eclipse phase, we have generated broadband spectra for PSR J1544+4937 at different orbital phases, namely, the NEP, FEP, EIP and EEP by splitting the observing band into smaller frequency slices. Different eclipse phases are shown in Figure 2. We divided the observing band into frequency slices of 10 MHz where the pulsar is still bright enough to potentially be detected in the NEP. In order to increase the signal-to-noise ratio during the brief ingress and egress phase we have averaged a 20 MHz bandwidth in both the EIP and EEP. The spectra at the NEP, FEP, EIP and EEP are shown in Figure 3.

2.5. Spectrum Modeling

We modeled the FEP spectrum ($F_{ec}(\nu)$) for free-free absorption, induced Compton scattering, and synchrotron absorption. We used the radiative transfer equation $F_{ec}(\nu) = F_{nonec}(\nu)e^{-\tau(\nu)}$ to model the FEP spectrum, where F_{nonec} is the power-law spectrum fitted to the observed NEP spectrum; which is taken to be constant throughout the orbit. $\tau(\nu)$ is the frequency dependent optical depth for different eclipse mechanisms

proposed by Thompson et al. (1994). We used the non-linear curve fitting function *curve_fit* of the *SciPy* package.

Analytical expressions of frequency dependent optical depths for the different mechanisms adopted from Thompson et al. (1994) are used in this study.

2.5.1. Free-Free Absorption

The radio emission from the pulsar can be absorbed by the free electrons of the eclipse medium by the free-free absorption. The free-free absorption optical depth is given by

$$\tau_{ff}(\nu) \approx 3.8 \times 10^{-14} \frac{f_{cl}}{T^{\frac{3}{2}} \nu^2 L} N_e^2 \ln(5 \times 10^{10} \frac{T^{\frac{3}{2}}}{\nu}) \quad (3)$$

where, T is the temperature of the eclipsing medium in Kelvin, N_e is the electron column density of the eclipse medium in cm^{-2} , $f_{cl} = \frac{\langle n_e^2 \rangle}{\langle n_e \rangle^2}$ is the clumping factor of the medium, and L is the absorption length in centimeters. Assuming a spherical distribution of eclipse medium around the companion, we consider the maximum absorption length; $L_{max} = 2R_E = 1.0R_\odot$ as twice of the eclipse radius; $R_E = 0.5R_\odot$. The observed FEP spectrum is fitted considering temperature, clumping factor, and absorption length as the free parameters using the expression for free-free optical depth in Equation 3. During fitting we put a physically motivated constraint that the temperature $T > 0$ and absorption length $L \leq L_{max}$.

2.5.2. Induced Compton Scattering

The induced Compton scattering optical depth is given by

$$\tau_{ind}(\nu) \approx 4 \times 10^6 \frac{N_e S_\nu}{\nu^2} \langle f(\phi) \rangle |\alpha + 1| (\frac{d_{kpc}}{a})^2 M \quad (4)$$

where S_ν is the mean flux density of the pulsar in millijanskys at frequency ν MHz, α is the spectral index of the incident radiation, d_{kpc} is the distance to the scattering center from the observer in kiloparsecs and $a \sim 1.2R_\odot$ (Bhattacharyya et al. 2013) is the distance between the companion and the pulsar in centimeters. $f(\phi)$ is an angular factor which is averaged out over the scattering region (Thompson et al. 1994). Reflection off a plasma cloud of radius of curvature R_C will cause de-magnification $M \sim (\frac{R_C}{2r})^2$, where r is the distance from the center of the curvature. The de-magnification factor varies between 0 and 1. We consider the NEP flux density as 6.5 ± 0.2 mJy. The distance to the binary system estimated from optical observations is 2–5 kpc (Tang et al. 2014) and we take the average value; $d_{kpc} = 3.5$ kpc. The spectral index at the NEP is α_{nonec}

$= -2.8 \pm 0.7$ and the distance between pulsar and companion is $a \sim 1.2R_\odot$ (Bhattacharyya et al. 2013). Considering these values and maximum de-magnification factor $M = 1$, we have calculated the induced Compton optical depth.

2.5.3. Cyclotron Absorption

Since the companion has a magnetic field, cyclotron absorption is another possible eclipse mechanism. The cyclotron frequency is $\nu_B = \frac{eB}{2\pi m_e c}$ and the corresponding cyclotron harmonic at frequency ν is $m = \frac{\nu}{\nu_B}$. There are two components of cyclotron optical depths for two polarization components of the incident radiation. One component optical depth (τ_{\parallel}) is parallel to the $(\vec{k} \times \vec{B}) \times \vec{k}$ and another component (τ_{\perp}) is perpendicular to the $(\vec{k} \times \vec{B}) \times \vec{k}$, where \vec{k} is the wavevector, \vec{B} is the magnetic field vector. Considering the LOS angle with the magnetic field is 90 degrees, τ_{\parallel} is very small compared to the τ_{\perp} at higher cyclotron harmonics. Thus, considering the LOS angle with the magnetic field is 90 degrees, the cyclotron absorption optical depth for perpendicular polarization component corresponding to cyclotron harmonic m is given by (Thompson et al. 1994) as

$$\tau_{abs \perp, \frac{\pi}{2}}^{(m)} = \frac{\pi}{2} \frac{m^{m+1}}{m!} \left(\frac{mk_B T}{2m_e c^2} \right)^{(m-1)} \frac{n_e e^2 L_B}{m_e c \nu} \quad (5)$$

where and $L_B = \left| \frac{ds}{dlnB} \right|$ is called the scale length of magnetic variation. For simplicity, we consider the scale length of electron density variations and magnetic field variations as similar. Thus, the quantity $n_e L_B$ is taken to be equal to the average electron column density N_e (Thompson et al. 1994). The cyclotron approximation is valid if the temperature $T \leq \frac{m_e c^2}{2km^3}$ (Thompson et al. 1994).

2.5.4. Synchrotron Absorption

In the trans-relativistic case, thermal electrons dominate the absorption if cyclotron harmonic is $m < \frac{1}{2}(p+1)$ (Thompson et al. 1994). Thus, thermal electrons dominate the absorption at lower cyclotron harmonics. At higher harmonics, we consider only the synchrotron absorption by nonthermal electrons with energy density distribution $n(E) = n_0 E^{-p}$; $E_{min} < E < E_{max}$. The optical depth is given by

$$\tau_{syn} = \left(\frac{3^{\frac{(p+1)}{2}} \Gamma(\frac{3p+2}{12}) \Gamma(\frac{3p+22}{12})}{4} \right) \left(\frac{\sin\theta}{m} \right)^{\frac{p+2}{2}} \frac{n_0 e^2}{m_e c \nu} L \quad (6)$$

where L is the absorption length and p is the power-law index. Here we have considered an average magnetic field strength along the LOS and homogeneous distribution nonthermal electron. We considered a tiny fraction

($\sim 1\%$) of total electron density (n_e) as a typical value of nonthermal electron density (Thompson et al. 1994). For a chosen value of LOS angle (θ) we fitted the observed spectrum with B and p as free parameters.

3. RESULTS

In this section we explore the eclipse mechanism and eclipse medium properties using the fitted broadband spectrum of the PSR J1544+4937 at different orbital phases around the superior conjunction.

3.1. Electron density at the Ingress/Egress Phase

The flux density drops to 85% of the NEP phase flux density at orbital phase $\phi_i = 0.16$ and $\phi_e = 0.30$, where ϕ_i and ϕ_e are defined as the start and end of the EIP and EEP respectively (Figure 2b). The orbital phase range $\phi_e - \phi_i$ corresponds to the eclipse radius $R_E \sim 0.5 R_\odot$. We observed the excess electron column density at the ingress and egress as $N_e \sim 1.0 \times 10^{16} \text{ cm}^{-2}$ (Figure 2a). Considering the constant electron density along the LOS, we estimate an average electron density; $n_e \approx 1.5 \times 10^5 \text{ cm}^{-3}$ at the eclipse boundaries (Polzin et al. 2018).

3.2. Frequency Onset of the Eclipse

Using the 10 MHz frequency slices, we find that in the FEP the pulsar is not detected above 5σ at frequencies below an eclipse onset frequency of $\nu_c = 345 \pm 5 \text{ MHz}$ where the pulsar has a flux density of $S_c = 1.1 \pm 0.2 \text{ mJy}$ (Figure 3a). The error on the eclipse onset frequency is defined as the half width of the frequency slice. The estimated eclipse onset is an order of magnitude more precise ν_c compared to previous estimates for any eclipsing MSP (Bhattacharyya et al. 2013; Polzin et al. 2019).

3.3. Observed Optical Depth at Eclipse Onset Frequency

Due to the large uncertainty of ν_c , previous studies could only put a limit on the physical parameters of the eclipse medium. With an order of magnitude of a more precise ν_c we can calculate the observed optical depth at the ν_c . We use an average value of the observed electron column density in the FEP of $N_e = 1.5 \times 10^{16} \text{ cm}^{-2}$ (Figure 2a). We calculate the optical depth $\tau_{\nu,c} \approx 1.7$ at ν_c since the flux density of the pulsar decreases from $6.5 \pm 0.2 \text{ mJy}$ in the NEP to $1.1 \pm 0.2 \text{ mJy}$ in the FEP (Figure 3a). This direct estimation of the optical depth at the FEP allows us to provide a strong constraint on the physical parameters of the eclipse medium, which was not possible before.

3.4. Broadband Spectra at Different Orbital Phases

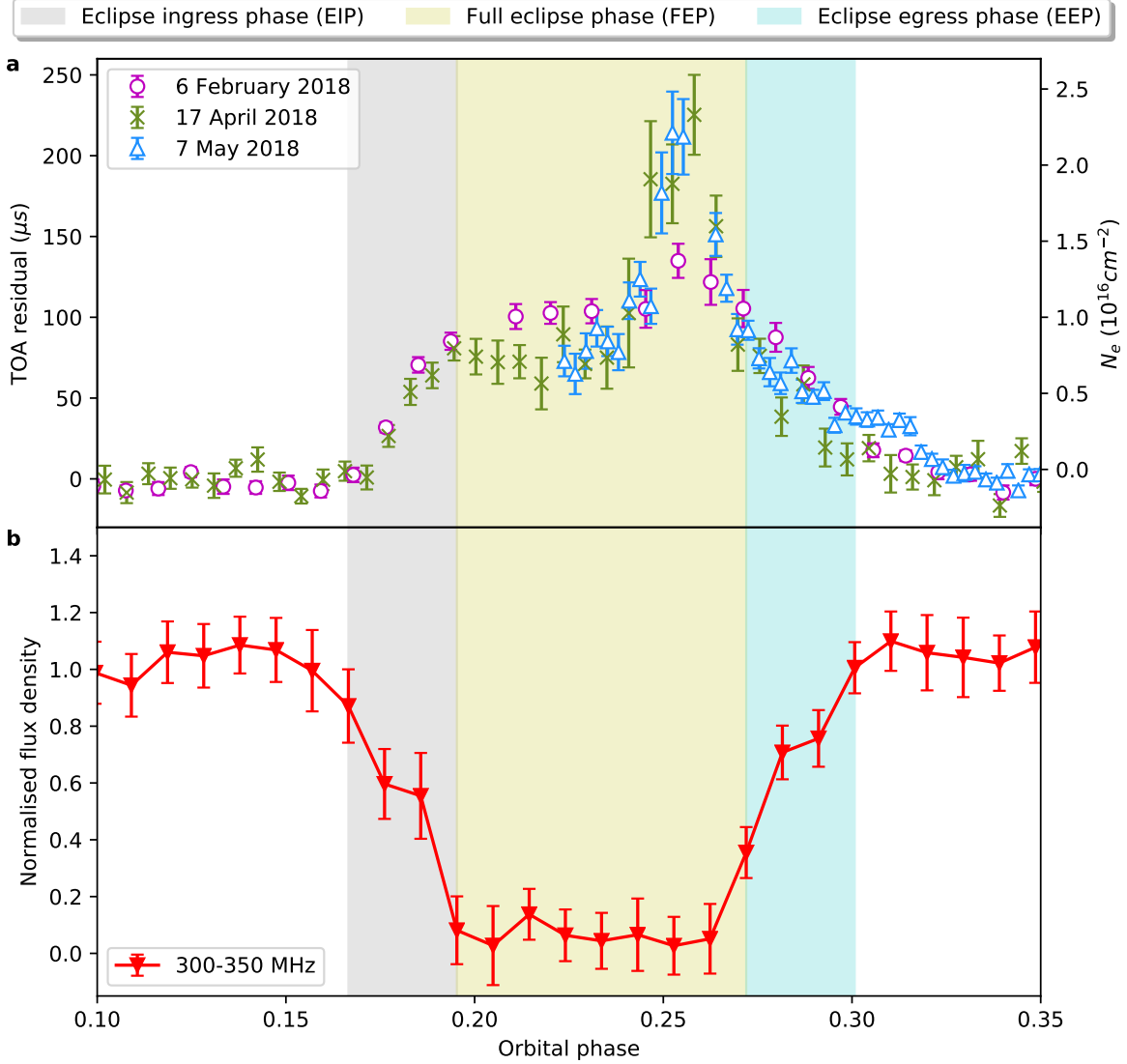


Figure 2. Variation of the excess electron column density (N_e) and the mean flux density with orbital phase around the superior conjunction. Considering the 300–350 MHz part of the band 3, the mean flux density drops to 85% of the NEP flux density at orbital phase 0.16 and continues to drop to the 5σ detection limit (1.1 mJy) at orbital phase 0.19. The orbital phase range 0.16–0.19 shaded by gray denotes the EIP. The flux density again increased above 5σ limit at orbital phase 0.27. The orbital phase range 0.19–0.27 shaded by yellow enotes the FEP. The flux density increased more than 85% of the NEP flux density at orbital phase 0.30. The orbital phase range 0.27–0.30 shaded by sky blue denotes the EEP. **(a)** The observed delay at the center frequency of band 3 (400 MHz) for the three different epochs is shown. The excess electron column density in the eclipse phase causes the observed delay in the pulse arrival time. **(b)** The mean flux density variation over 300–350 MHz normalized with respect to the NEP flux density is shown by red lower triangles.

At ν_c the eclipse medium is transitioning from an optically thick to thin regime which is hitherto unexplored for any other eclipsing MSP systems, since the majority of previous studies were performed at frequencies corresponding to the optically thick regime. In Figure 3a, we show the spectrum at the FEP and NEP for the observation on 2018 February 6. Fitting a power-law, $S_{nonec}(\nu) \propto \nu^{\alpha_{nonec}}$, where $\alpha_{nonec} = -2.8 \pm 0.7$ is the spectral index of the NEP spectrum. By comparison,

the spectrum in the FEP has a break in the spectrum. We fit a broken power law to the observed FEP spectrum given as

$$S(\nu) = \begin{cases} S_t \left(\frac{\nu}{\nu_t}\right)^{\alpha_{low}}, & \nu < \nu_t, \\ S_t \left(\frac{\nu}{\nu_t}\right)^{\alpha_{high}}, & \nu > \nu_t \end{cases} \quad (7)$$

where ν_t is the turnover frequency, S_t is the peak flux density at the turnover frequency ν_t , α_{low} is the spectral index for frequencies below ν_t and α_{high} is the spec-

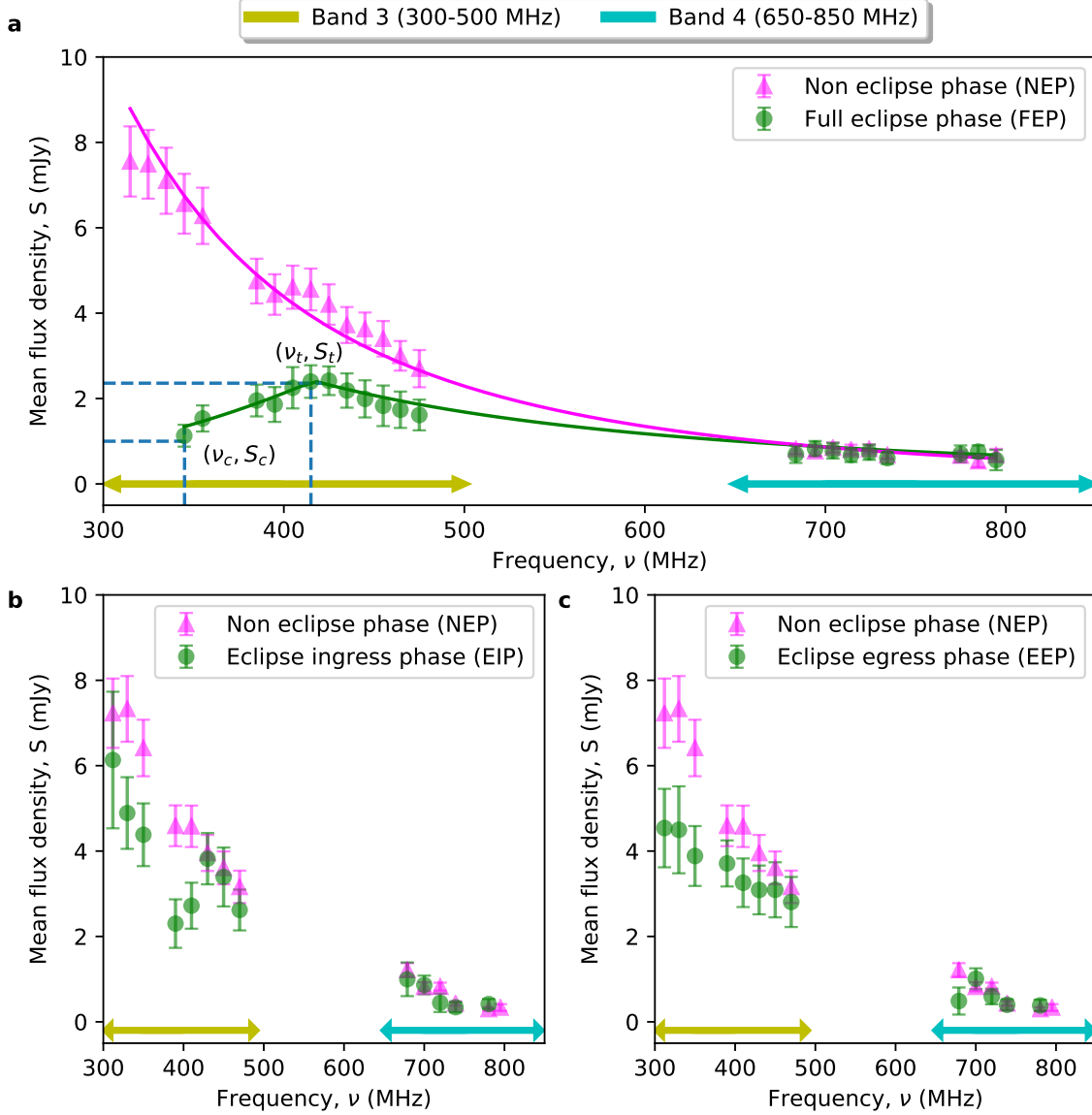


Figure 3. Spectral properties of the pulsed radio emission of the PSR J1544+4937 at the NEP, FEP, EIP, and EEP for the 2018 February 6 observation. The flux density as a function of frequency is shown. In all the plots the magenta points correspond to the mean flux densities measured at the NEP. The green points correspond to the mean flux densities measured in three eclipse regions; FEP (a), EIP (b), EEP (c). The span of the band 3 and band 4 are shown by the double headed arrows. Certain parts of the bands are masked due to the RFI or low sensitivity. (a) Fitted power law to the observed NEP spectrum is shown by the magenta solid line and the broken power law fitted to the observed FEP spectrum is shown by the green solid line. In the FEP the pulsar is not detected with a detection significance more than 5σ below $\nu_c = 345 \pm 5$ MHz. The flux density at ν_c is $S_c = 1.1 \pm 0.2$ mJy. In the FEP spectrum we can also see that there is a turnover at $\nu_t = 416 \pm 33$ MHz and the corresponding mean flux density is $S_t = 2.4 \pm 0.3$ mJy. (b),(c) The spectra at the EIP and EEP are different in characteristics compared to the spectrum at the FEP. In order to increase the signal-to-noise ratio during the brief ingress and egress phase, we averaged a 20 MHz bandwidth in both the EIP and EEP.

tral index for frequencies above ν_t . The fitted power law spectrum for the NEP is shown by magenta solid line and the fitted broken power law for the FEP is shown by the green solid line in Figure 3a. The errors on $\nu_t, \alpha_{low}, \alpha_{high}$ and S_t are the errors from fitting. Above a turn over frequency of $\nu_t = 416 \pm 33$ MHz the spectral index $\alpha_{high} = -1.9 \pm 0.2$ and below ν_t the spectrum has a positive spectral index, $\alpha_{low} = 3.1 \pm 0.1$. The peak flux density at ν_t obtained from broken power-law fit is $S_t = 2.4 \pm 0.3$ mJy. This difference between the NEP and the FEP spectral shape has not been reported before in any other eclipsing binary MSP. A comparison between the NEP spectrum with those in the EIP and the EEP are shown in the lower panels of Figure 3, and we can see that there are differences compared to the FEP spectrum suggesting that there may be different eclipse mechanisms in place in the different regions, or the physical properties of the material are sufficiently different.

3.5. Eclipse Mechanism

We consider different possible eclipse mechanisms (Thompson et al. 1994) to explain our observations (Section 2.5). Radiation at a frequency below the plasma frequency, $\nu_p = 8.5$ (n_e/cm^{-3}) kHz, of the eclipsing material will not be able to propagate through it. If we consider that the observed ν_c corresponds to ν_p in the FEP we find that the corresponding electron density is $n_{e,p} = 1.6 \times 10^9 \text{ cm}^{-3}$. This is in stark contrast to the electron density in the eclipse region, $n_e \sim 1.5 \times 10^5 \text{ cm}^{-3}$, estimated by assuming a spherically distributed eclipse medium and the electron densities derived from the delayed pulse arrival times (Figure 2a). This suggests that the eclipse onset at ν_c cannot be explained by the plasma frequency cutoff. On the other hand, radiation at frequencies higher than ν_p undergo refraction due to the intervening medium. If the angle of refraction is sufficiently large, the pulsed emission will be refracted out of the LOS resulting in an eclipse. If refraction is the cause of the observed eclipse at ν_c , the delay of the pulse arrival time at the eclipse boundaries is $\sim 10 - 100$ ms (Thompson et al. 1994), which is much larger than the observed delay in pulse arrival time at the eclipse boundaries $\sim 100 \mu\text{s}$ (Figure 2a). This suggests that the refraction at the frequencies below ν_c is not sufficient to explain the observed eclipse. Pulse broadening due to excess DM and scattering in the FEP is $\sim 45 \mu\text{s}$ at ν_c (Appendix A.3), which is less than the time resolution of the data, $81.92 \mu\text{s}$ and so it cannot reduce the observed pulse detection.

3.6. Modeled Spectrum

We have then modeled the spectrum in the FEP using the radiative transfer equation (Section 2.5) for three mechanisms: free-free absorption, induced Compton scattering and synchrotron absorption. We have assumed that the spectra at the NEP does not change for other reasons. We consider a given mechanism as the most plausible when the observed optical depth ($\tau_{\nu,c}$) and the observed FEP spectrum can be reproduced with physically acceptable parameters. We have modeled the FEP spectra for three different epochs to see whether eclipse mechanism or the eclipse medium properties varies significantly between epochs.

3.6.1. Free-Free absorption

The free-free absorption optical depth (τ_{ff}) [Equation 3] due to the free electrons in the eclipse medium depends on three physical quantities: temperature (T), absorption length (L) and clumping factor ($f_{cl} = \frac{\langle n_e^2 \rangle}{\langle n_e \rangle^2}$). Clumping factor is a measure of inhomogeneity of the medium. To obtain the observed value of $\tau_{\nu,c}$ from free-free absorption the temperature of the medium would need to be $T = 130 (f_{cl})^{\frac{2}{3}}$. Thus, either a very low temperature ($T \sim 1000$ K) or high clumping factor ($f_{cl} \sim 10^9$) is required to create an eclipse at ν_c due to free-free absorption. We fit (brown solid line in Figure 4a) the observed spectrum in the FEP (green circles in Figure 4a) using the frequency dependent optical depths of free-free absorption but did not obtain a good fit ($\chi_{red}^2 \sim 2$). The mismatch between the observed and modeled FEP spectrum suggests that the free-free absorption cannot produce the observed frequency dependent eclipses of PSR J1544+4937.

3.6.2. Induced Compton Scattering

Another possible eclipse mechanism is induced Compton scattering, which is a nonlinear scattering effect. Although the total number of incident photon remain conserved, this nonlinear scattering effectively changes the spectrum of the incident radiation and induces an optical depth (τ_{ind}) [Equation 4]. We have calculated $\tau_{ind} = 4 \times 10^{-2}$ at ν_c , which is two orders of magnitude smaller than the observed $\tau_{\nu,c}$. We have also modeled the observed spectrum in the FEP with induced Compton scattering considering the de-magnification factor can vary between 0 and 1. We have found that the model spectrum (blue solid line in Figure 4a) differs significantly to the observed FEP spectrum (green circles in Figure 4a). The corresponding reduced χ^2 is also very high; i.e. $\chi_{red}^2 \sim 46$.

3.6.3. Possibility of Cyclotron Absorption

Since the companion star and the pulsar wind have magnetic fields, we consider cyclotron absorption by

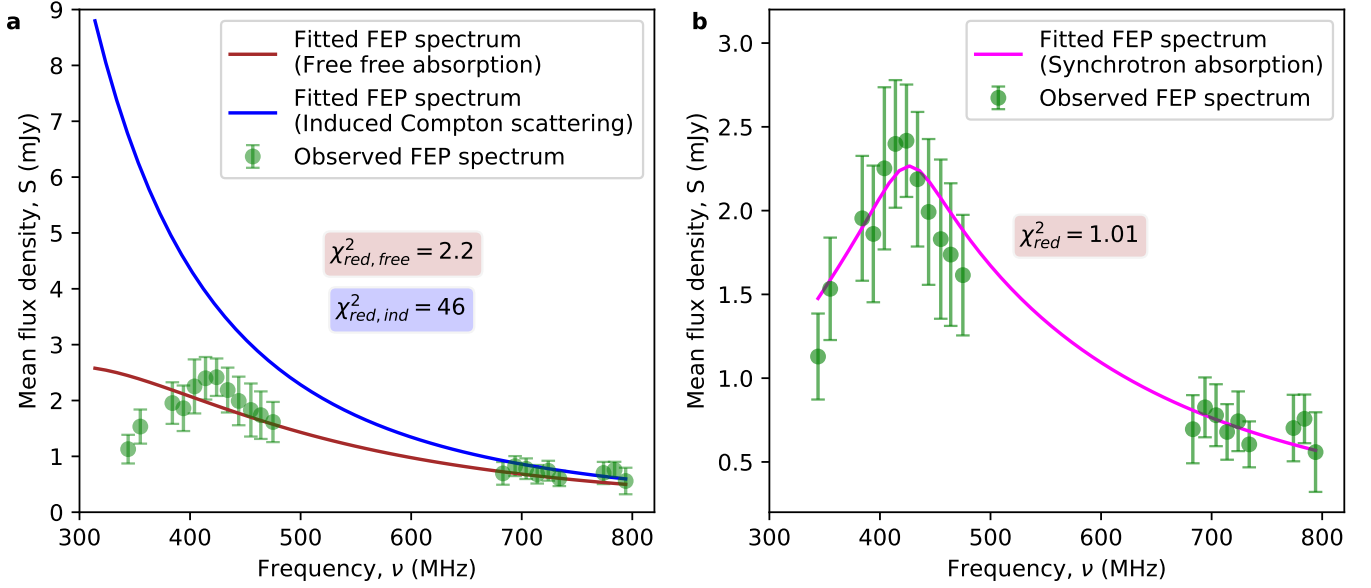


Figure 4. Observed FEP spectrum on 2018 February 6 fitted with the free-free absorption, the induced Compton scattering, and synchrotron absorption models. The observed FEP spectrum is shown by green circles in both the figures. (a) Fitted spectrum is shown by the brown solid line for the free-free absorption model and by the blue solid line for the induced Compton scattering. (b) The best-fit spectrum considering the synchrotron absorption by the relativistic electrons is shown by the magenta solid line. The observed FEP spectrum is well fitted with this model (the reduced chi-square is 1.01).

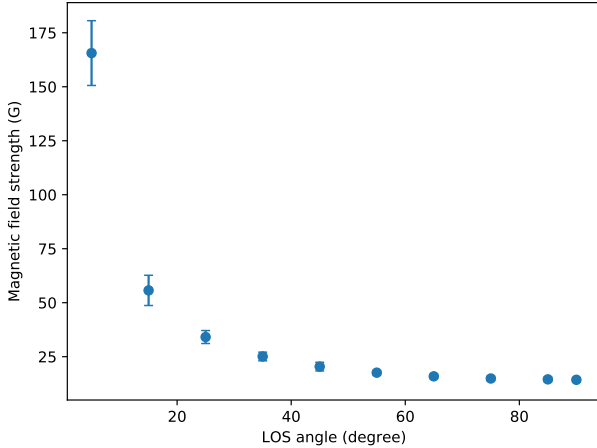


Figure 5. Estimated magnetic field strength considering different LOS angles. The average magnetic field strength estimated (B) during the fitting of the synchrotron model with the FEP spectrum has a degeneracy with the LOS angle (θ). While fitting the FEP spectrum for the 2018 February 6 observation, we vary the LOS angle between 5° and 90° in 10° step. We have kept the LOS angle fixed during each fitting and the corresponding estimated magnetic field strengths are shown in this figure.

nonrelativistic electrons as one of the possible eclipse mechanisms. Assuming an isotropic pulsar wind, we have estimated the characteristic magnetic field strength equating the magnetic pressure ($\frac{B^2}{8\pi}$) of the plasma of the eclipse medium to stagnation pressure of the incident

pulsar wind, $U_E = \frac{\dot{E}}{4\pi ca^2}$, where $\dot{E} = 1.15 \times 10^{34}$ erg/s is the spin down power of the pulsar and $a \sim 1.2 R_\odot$ is the distance between pulsar and companion. We have calculated the pulsar wind energy density; $U_E = 4.37$ erg/cm³ and the characteristic magnetic field strength is $B_E \approx 10$ G. The corresponding cyclotron frequency is $\nu_B \approx 30$ MHz and the cyclotron harmonic corresponding to ν_c is $m \approx 12$. This means that cyclotron absorption can only produce the observed eclipse at ν_c if the temperature is $T = 7.9 \times 10^7$ K [Equation 5]. However the cyclotron approximation is only valid for temperature $T \leq 1.7 \times 10^6$ K (Thompson et al. 1994). Thus, the required temperature is outside the range of cyclotron limit. Therefore, we rule out the cyclotron absorption by nonrelativistic electrons as the eclipse mechanism.

3.6.4. Synchrotron Absorption

In the trans-relativistic regime both the thermal and nonthermal electrons can contribute to the synchrotron absorption. Thermal electrons will dominate the absorption for lower cyclotron harmonic number $m < 4$ (Thompson et al. 1994) considering a nonthermal electron power-law index $p = 7$. But at higher cyclotron harmonic corresponding to ν_c ($m \approx 12$) the absorption by the thermal electrons is negligible. Thus, we have fitted the observed FEP spectrum considering only the synchrotron absorption by relativistic nonthermal electrons with the energy distribution $n(E) = n_0 E^{-p}$; $E_{min} < E < E_{max}$. We chose magnetic field strength

Date of obs	$B(\text{G})$	p
2018 February 6	14.0 ± 1.1	4.7 ± 0.6
2018 April 17	17.3 ± 1.1	5.6 ± 1.1
2018 May 7	9.9 ± 1.6	3.7 ± 0.8

Table 1. Note : Estimated physical parameters of the eclipse medium. Two physical parameters; the LOS averaged magnetic field strength (B) and p estimated during the fitting of the observed FEP spectrum are listed in this table. We consider the synchrotron absorption by relativistic non-thermal electrons following energy distribution $n(E) = n_0 E^{-p}$ as the eclipse mechanism. We considered the magnetic field is perpendicular to the LOS during the estimation of these parameters. The estimated parameters for three different epochs are broadly consistent.

$B = 1 \text{ G}$ and $p = 5$ as the initial guess values for performing the fitting. The modeled spectrum with synchrotron absorption (magenta solid line in Figure 4b) matches the observed spectrum in the FEP very well and the reduced χ^2 is also close to unity; $\chi_{red}^2 = 1.01$.

The FEP spectrum is therefore best modeled with synchrotron absorption by relativistic electrons as the eclipse mechanism for the observing epoch 2018 February 6. We have also performed spectral modeling for PSR J1544+4937 on two additional epochs, 2018 April 17 and 2018 May 7, and found that the best fits are also achieved by synchrotron absorption.

3.7. Estimated Physical Parameters of Eclipse Medium

While modeling the observed FEP spectrum with synchrotron absorption discussed in Section 3.6.4, we assumed that the nonthermal electron distribution in the eclipse medium is homogeneous and the average LOS angle to the magnetic field is 90° . Best-fit values of B and p for the three epochs are given in Table 1, which are broadly consistent. We obtain a mean value of magnetic field strength, $B \sim 13.7 \pm 1.2 \text{ G}$ across the three epochs, which is similar to the characteristic magnetic field strength B_E . We have estimated the nonthermal electron energy density, $U_{nth} \approx 10^{-4} \text{ erg/cm}^3$, which is only a tiny fraction of the total pulsar wind energy density, $U_E = 4.37 \text{ erg/cm}^3$. The estimated LOS averaged magnetic field strength using the synchrotron absorption model depends on the LOS angle (θ) with the magnetic field (Equation 6). To explore further we fit the FEP spectra for different values of θ between the range of $5^\circ - 90^\circ$ in 10° steps and the estimated values of B are shown in Figure 5. The upper and lower limits of the estimated LOS averaged magnetic field strengths are $162 \pm 14 \text{ G}$ and $14.0 \pm 1.1 \text{ G}$ respectively, which are also a similar order of magnitude to B_E .

4. DISCUSSION

This paper reports the very first modeling of the broadband radio spectra at the FEP to constrain the eclipse mechanism. We have found that the observed frequency dependent eclipses for PSR J1544+4937 can be well explained by synchrotron absorption by relativistic electrons, while the other mechanisms could not explain the observed eclipse (Section 3.5). We ruled out cyclotron absorption because the required temperature is much higher than the cyclotron limit for the observed optical depth at the ν_c . We find that the synchrotron absorption can reproduce the observed FEP spectra and also the estimated physical parameters are feasible. Thus, we conclude that the synchrotron absorption is the most plausible eclipse mechanism for PSR J1544+4937.

We have shown that the observed spectra at three different orbital phases (EIP, FEP and EEP) are significantly different (Section 2.4). This implies that the frequency dependence of the optical depth is varying as a function of orbital phase. Different frequency dependence of the optical depth for the EIP, FEP and EEP indicates that either eclipse mechanisms or the eclipse medium properties are varying with the orbital phase. Sensitive orbital phase resolved studies are needed to probe this in detail.

4.1. Fractional Contribution from Other Mechanisms

When considering the influence of the different eclipse mechanisms we assumed that the spectrum in the NEP is representative of that seen throughout the orbit, if there were no eclipse. Scintillation could change the flux density of the pulsar; however, the decorrelation bandwidth for diffractive scintillation is $\sim 1.1 \text{ kHz}$ (Section A.3) given the DM of the pulsar and thus will be averaged out over the 10 MHz frequency slices. Moreover, we would not expect scintillation to have this sort of orbital phase dependence. Although we have ruled out free-free absorption and induced Compton scattering as the main eclipse mechanism, we now consider if they may make a significant fractional contribution to the eclipses. Considering the average electron column density $N_e \sim 1.5 \times 10^{16} \text{ cm}^{-2}$ at the FEP, and a typical temperature of the stellar wind (Thompson et al. 1994); $T \sim 10^8 - 10^9 \text{ K}$ and clumping factor; $f_{cl} \sim 1$, we have estimated the free-free optical depth; $\tau_{ff} \sim 10^{-9} - 10^{-10}$ and the induced Compton scattering optical depth is $\sim 4 \times 10^{-2}$ at the ν_c . Thus, both free-free absorption and induced Compton scattering do not contribute significantly to the observed optical depth. Synchrotron absorption is therefore solely responsible for the observed frequency dependent eclipsing and the estimated physical param-

eters are not affected by a contribution to the optical depth by other mechanisms.

4.2. Comparison of Estimated Magnetic Field Strength with Previous Studies

Most previous studies (Fruchter et al. 1990; Polzin et al. 2018; Fruchter et al. 1988; Polzin et al. 2020; Stappers et al. 1998; Polzin et al. 2019) have concluded that the low frequency eclipses may be caused by cyclotron/synchrotron absorption. The magnetic field strength, B , is a crucial parameter for cyclotron/synchrotron absorption. Recent studies of PSR B1957+20 (Li et al. 2019) and PSR J2256–1024 (Crowter et al. 2020) estimated B of a few milligauss at the eclipse boundaries, which is significantly different from B_E and insufficient to cause cyclotron absorption at the observing frequency. However, recent polarization observations of PSR J2051–0827 (Polzin et al. 2019) using the Parkes UWL (Hobbs et al. 2020) at the FEP provides a limit on the parallel component $B_{\parallel} = 20 \pm 120$ G of the magnetic field, which is close to the characteristic magnetic field strength for this pulsar. Our estimate of the magnetic field strength, using a completely different method for PSR J1544+4937, is consistent with B_E . Thus, the measurement of a very low magnetic field strength at the eclipse boundaries were possibly due to the observations at the eclipse boundaries where the eclipse medium properties may be significantly different than in the FEP (Khechinashvili et al. 2000).

4.3. Future Applications on Broad Range of Binaries

Our new method can be utilized to understand the eclipse mechanisms and the evolution of other eclipsing MSPs in compact binaries, including the transitional MSP J1227–4853 (Roy et al. 2015; Kudale et al. 2020). In the future more sensitive observations will allow us to perform the spectral modeling with higher orbital phase resolution covering the eclipse region. This method can also be used for a diverse range of binaries, with different companion types and orbital properties, for which spectral modulation and DM variation with orbital phase is, or expected to be, observed. For example, this method can probe the eclipse properties of PSR B1259–63 (Johnston et al. 2005), which is orbiting a massive Be star and the observed eclipses are thought to be caused by the circumstellar disk of the Be star and related systems, such as PSR J1740–3052 (Madsen et al. 2012). For the double pulsar binary, PSR J0737–3039, where the observed flux density of one pulsar is modulated by the second pulsar (Lyne et al. 2004; McLaughlin et al. 2004; Breton et al. 2012), an adoption of our simultaneous broadband observing approach may be used to probe the magnetosphere of the second one. Thus, even though primarily developed for the study of the eclipse properties of the MSPs in compact orbits, this technique has the potential to probe the stellar environment for a wide range of binaries via the modeling of broadband radio spectra.

APPENDIX

A. APPENDIX

The method for flux calibration and estimation of mean flux densities are described in Appendix A.1 and Appendix A.2 respectively. We describe the calculation of the effect of pulse broadening and scintillation on the observed pulse width in Appendix A.3.

A.1. Flux calibration

Flux calibration of the pulsar is performed using the on source scan of a standard flux calibrator source 3C 286 and off source scan at 5° away from the flux calibrator to convert the data into physical flux density unit Jansky. We have used the following relation to calculate the sensitivity of the phased array for each 1 MHz frequency chunk for the 200 MHz band:

$$\frac{P_{on} - P_{off}}{P_{off}} = S_{cal} \frac{G}{T_{sys}} \quad (\text{A1})$$

where P_{on} is the mean power for the scan on 3C 286 and P_{off} is the mean power while pointing the antennas at

the cold sky 5° off from 3C 286, T_{sys} is the overall system temperature in Kelvin, S_{cal} is the flux density of calibrator source in jansky and G is the antenna gain in Kelvins per jansky. We then multiply each 1 MHz frequency bin of baseline subtracted incoherently dedispersed and folded pulsar dataset with $\frac{T_{sys}}{G}$ estimated using Equation A1 to obtain a flux calibrated dataset.

A.2. Calculating the Mean Flux Density

The mean flux density is obtained as the area under the pulse profile divided by the number of pulse phase bin (n_{bin}) in the pulse profile. We have accounted for the variable pulse width across frequency while calculating the mean flux density. The total error on the mean flux density is calculated as a quadratic sum of the off pulse rms noise (σ_{off}) scaled to the number of pulse phase bins in the profile ($\sigma = \frac{\sigma_{off}}{\sqrt{n_{bin}}}$) and a 10% (f_{err}) flux scale uncertainty (Chandra & Kanekar 2017). Thus,

total error on the mean flux density is

$$\sigma_{total} = \sqrt{\sigma^2 + (f_{err} \times S_{psr})^2} \quad (\text{A2})$$

where S_{psr} is the mean flux density of the pulsar.

A.3. Pulse Broadening and Scintillation

The intrinsic pulse width of the pulsar radio emission gets broadened due to the dispersion and scattering. The effective pulse width is the quadratic sum of the intrinsic pulse width ($t_{intrinsic}$), pulse broadening due to dispersion measure (t_{DM}) and scattering (t_s). The effective pulse width can also be expressed in terms of the observed pulse profile as,

$$t_{eff} = \sqrt{t_{intrinsic}^2 + t_{DM}^2 + t_s^2} = \frac{S_{mean}}{S_{peak}} P \quad (\text{A3})$$

where S_{mean} is the mean flux density, S_{peak} is the peak flux density, and P is the pulsar rotation period. We have estimated the effective pulse width at 345 MHz is 345 μ s. To obtain the scattering time scale we have assumed that the intrinsic pulse width is 10% of the pulse period, $t_{intrinsic} = 215.9 \mu$ s. Pulse broadening due intra-channel dispersion for finite channel width of 48.28

kHz is $t_{DM} = 228 \mu$ s. Thus, using Equation A3, the estimated value of the scattering timescale is $t_s \approx 141 \mu$ s and corresponding decorrelation bandwidth is $\Delta f = \frac{1}{2\pi t_s} \sim 1.1$ kHz.

Software: GPTOOL (Chowdhury et al., in preparation)

DSPSR¹ (van Straten & Bailes 2010)

TEMPO2² (Hobbs et al. 2006; Edwards et al. 2006)

PSRCHIVE³ (W. Hotan et al. 2004)

scipy⁴ (Virtanen et al. 2020)

Facilities: GMRT(Gupta et al. 2017)

We acknowledge support of the Department of Atomic Energy, Government of India, under project no.12-R&D-TFR-5.02-0700. The GMRT is run by the National Centre for Radio Astrophysics of the Tata Institute of Fundamental Research, India. We thank the staff of the GMRT who have made these observations possible. We thank the anonymous reviewer for insightful comments and suggestions. D.K. acknowledge discussion with Aditya Chowdhury (NCRA-TIFR).

REFERENCES

- Benvenuto, O. G., Vito, M. A. D., & Horvath, J. E. 2014, The Astrophysical Journal, 786, L7, doi: [10.1088/2041-8205/786/1/17](https://doi.org/10.1088/2041-8205/786/1/17)
- Bhattacharya, D. 1996, in IAU Colloq. 160: Pulsars: Problems and Progress, Astronomical Society of the Pacific Conference Series, 547
- Bhattacharyya, B., Roy, J., Ray, P. S., et al. 2013, The Astrophysical Journal, 773, L12, doi: [10.1088/2041-8205/773/1/112](https://doi.org/10.1088/2041-8205/773/1/112)
- Breton, R. P., Kaspi, V. M., McLaughlin, M. A., et al. 2012, The Astrophysical Journal, 747, 89, doi: [10.1088/0004-637x/747/2/89](https://doi.org/10.1088/0004-637x/747/2/89)
- Chandra, P., & Kanekar, N. 2017, The Astrophysical Journal, 846, 111, doi: [10.3847/1538-4357/aa85a2](https://doi.org/10.3847/1538-4357/aa85a2)
- Crowter, K., Stairs, I. H., McPhee, C. A., et al. 2020, Monthly Notices of the Royal Astronomical Society, 495, 3052
- Edwards, R. T., Hobbs, G. B., & Manchester, R. N. 2006, Monthly Notices of the Royal Astronomical Society, 372, 1549
- Freire, P. C. C. 2005, in Astronomical Society of the Pacific Conference Series, Vol. 328, Binary Radio Pulsars, ed. F. A. Rasio & I. H. Stairs, 405
- Fruchter, A. S., Berman, G., Bower, G., et al. 1990, The Astrophysical Journal, 351, 642, doi: [10.1086/168502](https://doi.org/10.1086/168502)
- Fruchter et al., A. 1988, The Nature Letters, 333, 237
- Gupta, Y., Ajithkumar, B., Kale, H., et al. 2017, Current Science, 113, 707, doi: [10.18520/cs/v113/i04/707-714](https://doi.org/10.18520/cs/v113/i04/707-714)
- Hobbs, G., Manchester, R. N., Dunning, A., et al. 2020, Publications of the Astronomical Society of Australia, 37
- Hobbs, G. B., Edwards, R. T., & Manchester, R. N. 2006, Monthly Notices of the Royal Astronomical Society, 369, 655
- Johnston, S., Ball, L., Wang, N., & Manchester, R. N. 2005, Monthly Notices of the Royal Astronomical Society, 358, 1069, doi: [10.1111/j.1365-2966.2005.08854.x](https://doi.org/10.1111/j.1365-2966.2005.08854.x)
- Khechinashvili, D. G., Melikidze, G. I., & Gil, J. A. 2000, ApJ, 541, 335, doi: [10.1086/309408](https://doi.org/10.1086/309408)
- Kudale, S., Roy, J., Bhattacharyya, B., Stappers, B., & Chengalur, J. 2020, The Astrophysical Journal, 900, 194, doi: [10.3847/1538-4357/aba902](https://doi.org/10.3847/1538-4357/aba902)

¹ See <http://dspsr.sourceforge.net/>

² See <https://bitbucket.org/psrsoft/tempo2/src/master/>

³ See <http://http://psrchive.sourceforge.net>

⁴ https://docs.scipy.org/doc/scipy/reference/generated/scipy.optimize.curve_fit.html

- Li, D., Lin, F. X., Main, R., et al. 2019, *Monthly Notices of the Royal Astronomical Society*, 484, 5723
- Lorimer, D. R., & Kramer, M. 2004, *Handbook of Pulsar Astronomy*, Vol. 4 (Cambridge University Press)
- Lyne, A. G., Manchester, R. N., D'Amico, N., et al. 1990, *The Nature*, 347, 650, doi: [10.1038/347650a0](https://doi.org/10.1038/347650a0)
- Lyne, A. G., Burgay, M., Kramer, M., et al. 2004, *Science*, 303, 1153, doi: [10.1126/science.1094645](https://doi.org/10.1126/science.1094645)
- Madsen, E. C., Stairs, I. H., Kramer, M., et al. 2012, *Monthly Notices of the Royal Astronomical Society*, 425, 2378, doi: [10.1111/j.1365-2966.2012.21691.x](https://doi.org/10.1111/j.1365-2966.2012.21691.x)
- McLaughlin, M. A., Kramer, M., Lyne, A. G., et al. 2004, *The Astrophysical Journal Letters*, 613, L57, doi: [10.1086/424998](https://doi.org/10.1086/424998)
- Polzin, E. J., Breton, R. P., Bhattacharyya, B., et al. 2020, *Monthly Notices of the Royal Astronomical Society*, 494, 2948, doi: [10.1093/MonthlyNoticesoftheRoyalAstronomicalSociety/staa596](https://doi.org/10.1093/MonthlyNoticesoftheRoyalAstronomicalSociety/staa596)
- Polzin, E. J., Breton, R. P., Stappers, B. W., et al. 2019, *Monthly Notices of the Royal Astronomical Society*, 490, 889–908, doi: [10.1093/MonthlyNoticesoftheRoyalAstronomicalSociety/stz2579](https://doi.org/10.1093/MonthlyNoticesoftheRoyalAstronomicalSociety/stz2579)
- Polzin, E. J., Breton, R. P., Clarke, A. O., et al. 2018, *MNRAS*, 476, 1968, doi: [10.1093/MonthlyNoticesoftheRoyalAstronomicalSociety/sty349](https://doi.org/10.1093/MonthlyNoticesoftheRoyalAstronomicalSociety/sty349)
- Roberts, M. S. E. 2013, in *Neutron Stars and Pulsars: Challenges and Opportunities after 80 years*, ed. J. van Leeuwen, Vol. 291, 127–132
- Roy, J., Gupta, Y., Pen, U.-L., et al. 2010, *Experimental Astronomy*, 28, 25, doi: [10.1007/s10686-010-9187-0](https://doi.org/10.1007/s10686-010-9187-0)
- Roy, J., Ray, P. S., Bhattacharyya, B., et al. 2015, *The Astrophysical Journal*, 800, L12, doi: [10.1088/2041-8205/800/1/112](https://doi.org/10.1088/2041-8205/800/1/112)
- Stappers, B. W., Bailes, M., Manchester, R. N., Sandhu, J. S., & Toscano, M. 1998, *The Astrophysical Journal*, 499, L183, doi: [10.1086/311382](https://doi.org/10.1086/311382)
- Swarup, G. 1991, in *Astronomical Society of the Pacific Conference Series*, Vol. 19, IAU Colloq. 131: Radio Interferometry. Theory, Techniques, and Applications, 376–380
- Tang, S., Kaplan, D. L., Phinney, E. S., et al. 2014, *The Astrophysical Journal*, 791, L5, doi: [10.1088/2041-8205/791/1/L5](https://doi.org/10.1088/2041-8205/791/1/L5)
- Thompson, C., Blandford, R. D., Evans, C. R., & Phinney, E. S. 1994, *The Astrophysical Journal*, 422, 304, doi: [10.1086/173728](https://doi.org/10.1086/173728)
- van Straten, W., & Bailes, M. 2010, *DSPSR: Digital Signal Processing Software for Pulsar Astronomy*
- Virtanen, P., Gommers, R., Oliphant, T. E., et al. 2020, *Nature Methods*, 17, 261, doi: [10.1038/s41592-019-0686-2](https://doi.org/10.1038/s41592-019-0686-2)
- W. Hotan, A., van Straten, W., & N. Manchester, R. 2004, *Publications of the Astronomical Society of Australia*, 21, 302, doi: [10.1071/AS04022](https://doi.org/10.1071/AS04022)